Statistics and analysis of high-altitude wind above the western Tibetan Plateau

Xuan Qian [1]★ Yongqiang Yao,[1] Hongshuai Wang,[2] Lei Zou[3] and Yao Li[1,4]

[1]*National Astronomical Observatories of China, Chinese Academy of Sciences, 20A Datun Road, Chaoyang District, Beijing 100101, China*
[2]*Kaiyang Space Technology Co. Ltd, No. 8 Malianwa North Road, Haidian District, Beijing 100085, China*
[3]*Key Laboratory of Water Cycle and Related Land Surface Processes, Institute of Geographic Sciences and Natural Resources Research, Chinese Academy of Sciences, No. 11 Datun Road, Chaoyang District, Beijing 100101, China*
[4]*University of Chinese Academy of Sciences, 19A Yuquan Road, Shijingshan District, Beijing 100049, China*

ABSTRACT

This article aims at studying the characteristics of high-altitude wind at the Ali Observatory on the western Tibetan Plateau, as the high-altitude wind has been put forward as a critical parameter for site evaluation, especially for adaptive optics. We have run a meso-scale numerical weather research and forecasting (WRF) model in three nested domains with different horizontal resolutions, centred at the Ali Observatory; the model results with the highest horizontal resolution of 1 km and temporal resolution of 0.5 h are presented, and also statistical analyseis of vertical wind profiles and 200 hPa wind speed are performed. Moreover, comparisons of wind speeds obtained from model and radiosoundings are presented; as the vertical resolution has been proved to be key to the estimation of optical turbulence with meso-scale models, the vertical resolutions are both set to 50 m for wind profiles, which reveals a high level of agreement and provides a useful tool for site assessment. The results prove the good character of the high-altitude wind over the Ali region, especially in summer half year, with a yearly median 200 hPa wind speed of 33.6 m s^{-1} in 2016, and also provide proof of the potential advantage of the Ali Observatory for adaptive optics. Furthermore, we certify that meso-scale models can offer dependable estimation of high-altitude wind over the Tibetan Plateau; the wind simulations provided by the WRF model will be of great benefit for adaptive optics, which also provides the vertical distributions of $C_N{}^2$ and τ_0 above astronomical observatories.

Key words: atmospheric effects – methods: numerical – methods: data analysis – site testing.

1 INTRODUCTION

The characteristics of the vertical wind speed profile over an astronomical observatory are of great significance. Near the ground surface layer, a strong wind may introduce oscillations of the dome and the telescope, affecting the image quality of the telescope; the vertical wind speed is also closely related to atmospheric optical turbulence. A large wind speed and its shear of speed gradient are indicators of atmospheric turbulence, which, in association with stable atmospheric stratification (a positive potential temperature gradient), generates optical turbulence that affects the resolution of ground-based astronomical observations above the site; furthermore, the stronger the wind, the faster the turbulence layers pass through the pupil of a telescope, and the higher the frequency of the adaptive optics system to correct the turbulence perturbations in the wavefront (Chueca et al. 2004; Hagelin, Masciadri & Lascaux 2010).

As one of the fundamental elements for astronomical site testing, the vertical wind speed is always used to evaluate the application conditions of adaptive optics for large ground-based telescopes. The resolving power of a ground-based telescope and image quality depend on the strength of the atmospheric optical turbulence. The

adaptive optical (AO) system is necessary equipment for large ground-based telescopes to compensate for the effects of atmospheric turbulence, and to bring the resolution of telescope imaging close to the diffraction limit. The characteristics of the whole layer of atmospheric turbulence need to be known in detail for the design and effective operation of the AO system, so the atmospheric turbulence at an observatory site needs to be monitored for a long time. For a correlation between the maximum source of turbulence and the peak value of the wind speed profile, estimations on atmospheric turbulence parameters using wind speed profiles have been put forward (Sarazin & Tokovinin). Large vertical gradients are associated with the development of the Kelvin–Helmholtz instability and the formation of turbulence. One of the most important characteristics of the optical turbulence is the turbulence velocity (V_0), which is often determined by the wind speed at a pressure level of 200 hPa (V_{200}); the height of this level coincides with the position of the jet stream at an altitude of about 12 km (associated with large vertical gradients of the horizontal velocity of the airflow) (Sarazin & Tokovinin 2001). The suitability of a site for astronomical observations at high resolution is often assessed using information on V_{200} and this information is used to make recommendations for the AO system. Thus, the analysis of the wind speed at the height of the 200 hPa pressure level (200 hPa wind speed) can be used to evaluate the applicability of the AO system for site testing, as in northern Chile; there is a good linear

★ E-mail: qianxuan@nao.cas.cn

relationship between the mean V_0 and V_{200} at 200 hPa pressure in the tropopause:

$$V_0 = 0.4 \times V_{200} \tag{1}$$

and the atmospheric coherence time (τ_0) is inversely proportional to the mean turbulence speed ($\tau_0 = 0.31 \times r_0/V_0$) (Roddier 1981, 1982).

The wavefront coherence time is an astro-climatic parameter that depends on the optical turbulence and wind speed:

$$\tau_0 = 0.057\lambda^{\frac{6}{5}} \left[\int_0^\infty V(h)^{\frac{5}{3}} C_N{}^2(h)\mathrm{d}h \right]^{\frac{-3}{5}}, \tag{2}$$

which is equivalent to

$$\tau_0 = 0.31\frac{r_0}{V_0}. \tag{3}$$

Here, r_0 is the Fried parameter and V_0 is the equivalent velocity:

$$V_0 = \left[\frac{\int_0^\infty V(h)^{\frac{5}{3}} C_N{}^2(h)\mathrm{d}h}{\int_0^\infty C_N{}^2(h)\mathrm{d}h} \right]^{\frac{3}{5}}. \tag{4}$$

Therefore, τ_0 depends on the vertical wind speed $V(h)$ and the strength of the optical turbulence $C_N{}^2$. For calculating the wavefront coherence time τ_0, Sarazin & Tokovinin () put forward an empirical correlation between V_0 and V_{200} ($V_0 = \max(V_{ground}, 0.4 \times V_{200})$) in northern Chile, and for other sites, Masciadri & Egner (2006) summarized that the wind speed profiles in the troposphere are essential, so full wind speed profiles are absolutely essential for characterizing an observatory, such as for the calculation of τ_0 (Hagelin et al. 2010).

Masciadri (2003), Masciadri, Lascaux & Fini (2013) have demonstrated that a meso-scale model with a horizontal resolution of 1 km can provide much better estimations of the atmospheric parameters above mid-latitude astronomical sites; they have presented an overview of the MOdelling ESO Sites project that aims at proving the feasibility of atmospheric parameters such as wind speed and optical turbulence at Cerro Paranal and Cerro Armazones. The vertical distributions of wind speed at Mt Graham, the site of the Large Binocular Telescope, obtained using operational analyses both from the ECMWF model and from the Meso-NH model, have proved that a meso-scale model can provide reliable estimations of vertical wind speed above astronomical sites from the ground up to the top of the atmosphere (Hagelin et al. 2010). The atmospheric model Meso-NH has been used to provide very good consistency with radiosonde observations, which can be considered as an independent reference (Sivo et al. 2018). These all make us think that meso-scale numerical models can be a reliable tool to obtain the characteristics of the vertical wind speed, especially above the Tibetan Plateau with complex terrain.

In this article, we present the characteristics of the vertical wind speed on a time-scale of 1 yr at the Ali Observatory above the western Tibetan Plateau with complex terrain, using a meso-scale numerical WRF (weather research and forecasting) model. The Ali Observatory, which is located at (32.30°N, 80.05°E) at an altitude of 5050 m in the south-west area of the Tibetan Plateau, is a new observatory constructed in western China. Long-term measurement and study of the atmospheric characteristics above the high Ali show that the Ali area is indeed a place with large atmospheric stability, very low humidity, little cloud and low pollution, and that the high altitude has potential advantages for multi-waveband observations (Zhang et al. 2010; Qian 2011; Yao et al. 2012; Zhang et al. 2012; Wang et al. 2012; Qian et al. 2015, 2018, 2019). The Ali Observatory

has been proposed as a candidate site for many projects, such as the Chinese Large Optical Telescope, the East Asia Observatory, the Thirty Meter Telescope, the Northern Cherenkov Telescope Array, and so on (Qian et al. 2019). For assessments of the site for large optical telescope projects, the high-altitude wind conditions above the Ali Observatory need to be determined as soon as possible.

This paper is part of a series reporting on the results of the site assessment of the Ali Observatory and is structured as follows: Section 2 describes the WRF model, the initial and boundary conditions and the configuration used in the model simulation. The vertical wind speed at the Ali Observatory is discussed in Section 3 and compared with the results from the radiosoundings. Section 4 presents the results of the 200 hPa wind speed above the western Tibetan Plateau, and also the 200 hPa wind at the Ali Observatory and at the Indian Astronomical Observatory, Hanle, which is about 110 km from the Ali Observatory. Finally, our conclusions are presented in Section 5.

2 MODEL CONFIGURATION

In this study, we make use of the WRF version 3.7 to obtain the characteristics of vertical wind speed in a three-layer nested region centred at the Ali Observatory in 2016. The WRF model is a meso-scale numerical weather prediction system designed for atmospheric research and operational forecasting applications (Jordan et al. 2015), which has advantages in portability, ease of maintenance, expandability, high efficiency, convenience, multiple nesting and the ability to be easily located in different geographical locations. It is also a completely compressible non-statics model, the Arakawa C grid points are applied in the horizontal direction, and the terrain follows mass coordinates in the vertical direction. In terms of time integration, a third-order or fourth-order Runge–Kutta algorithm is adopted (http://www.mmm.ucar.edu/wrf/users/). From the NCAR and NCEP websites, the source code, the required terrain and weather data for the WRF model can be downloaded. At present, many astronomers have devoted themselves to using this model to analyse the characteristics of atmospheric elements relevant to astronomical observations at different wavelengths, especially for those over large areas, with long time series, and where it is difficult to measure. By using the numerical model, analytical results with high resolution can be obtained through the accurate schemes of various kinds of models, which can provide a reliable basis for the evaluation of astronomical sites.

Fig. 1 gives different domain sets for the WRF configuration in this study. There are three nested domains, and the centre is at the Ali Observatory (80.08°E, 32.30°N, 5050 m above sea level). The spatial resolution of the innermost domain 03 (d03) is 1.0×1.0 km, the inter-layer (d02) resolution is 3.0×3.0 km, and the outermost (d01) horizontal resolution is 9.0×9.0 km, as shown in Table 1. There are 34 vertical levels, from the ground to the height of the 20 hPa pressure level, and the height of the WRF output is represented by the Sigma coordinate. When the model is running, the outermost domain provides accurate boundary data to the inside domain, as the coverage of the outermost domain is large and the resolution is low, which can also enhance the computer velocity.

The Tibetan Plateau lies in the subtropical central and eastern part of the continent of Eurasia, and is the highest plateau in the world with complex topography. Ali is located at the south-west border of China, the northern part of the Tibetan Plateau, and the western part of the Tibet Autonomous Region, with a mean altitude above 4500 m; the climatic type is the temperate monsoon arid climate of the plateau. The PBL (planetary boundary layer) scheme for regional climate models is of great significance; its
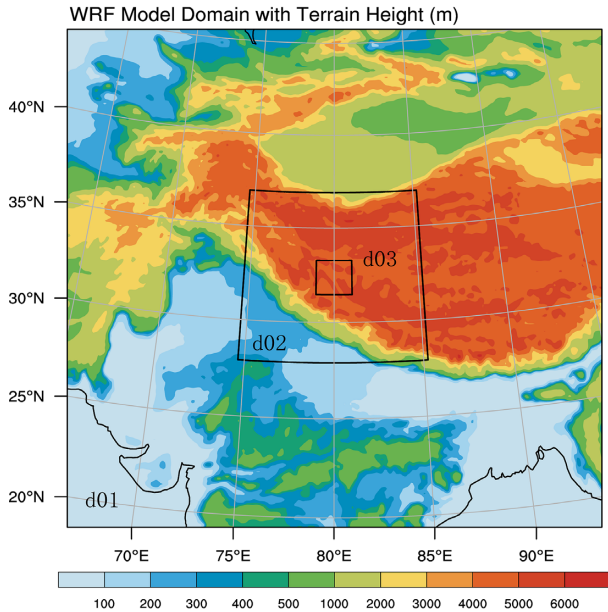
Figure 1. The three nested domains in the WRF model configuration, centred at the Ali Observatory (80.08°E, 32.30°N, 5050 m above sea level).

Table 1. The three nested domains used for the WRF configuration. *nx* and *ny* are the number of grid points in the east–west (E–W) and north–south (N–S) directions, *dx* and *dy* are the horizontal resolutions in the E–W and N–S directions, respectively.

Domain	*dx* (km)	*nx*	*dy* (km)	*ny*	Area × 10^4 (km^2)
d01	9.0	201	9.0	101	625
d02	3.0	101	3.0	101	25
d03	1.0	101	1.0	201	4

uncertainty can cause large systematic deviations of the regional climate model. The characteristics of PBL on the Tibetan Plateau are unique. In the Ali area, the average elevation is high, the sunshine is strong, and there are numerous mountains, with complex and highly undulating terrain, and the distribution of surface vegetation is not uniform (the main types of vegetation are alpine meadow and shrub, Yang 2008); in addition, the underlying surface is a combination of thermal non-uniformity and dynamic non-uniformity, so the surface heating in the zone has spatial inhomogeneity (Li et al. 2017; Xu et al. 2018). According to the specific topographical, environmental and meteorological characteristics of the plateau, all simulations are performed for the Ali area using the WRF single-moment six-class (WSM6) cloud microphysics scheme, the NOAH land-surface model, the Dudhia shortwave radiation, the Grell–Devenyi (GD) convective scheme, and the rapid radiative transfer model (RRTM) for long-wave radiation, and for the local turbulent kinetic energy scheme, the MYJ (Mellor–Yamada–Janjic) PBL scheme is selected (https://www2.mmm.ucar.edu/wrf/users/docs/user_guide_V3.7/).

For the boundary conditions and initial conditions, we make use of the ERA-Interim reanalysis data sets, which have high credibility, for the plateau, released by the European Center for Medium-Range Weather Forecasts (ECWMF) for the WRF model configuration, with a horizontal resolution of 0.75 × 0.75°, and the output times of the data are at Beijing Time (BT) 00:00 (UTC 18:00), BT 06:00 (UTC 00:00), BT 12:00 (UTC 06:00) and BT 18:00 (UTC 12:00) each day (http://www.ecmwf.int/en/forecasts/datasets/archive-datasets/reanalusis-datasets/era-interim/). Simulations from 2015
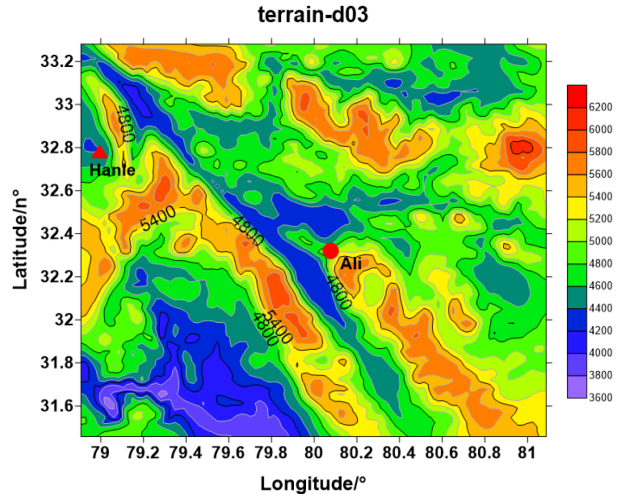

Figure 2. The terrain of domain 03 around the Ali Observatory with a resolution of 1 km; the coverage is about 200 × 200 km. The centre is at the Ali Observatory (80.08°E, 32.30°N, 5050 m above sea level).

December 31 to 2016 December 31 start at BT 18:00 (UTC 12:00) the day before with 30 h of integration in each day; the first 6 h can be considered as the spin-up time of the model, which can be deleted, and the output data of the last 24 h are kept for analysis. For domain 02, the output data are kept every hour, and every half hour for domain 03. When the model is running, grid nudging is performed in domain 01 for the wind (u/v), temperature (t) and humidity (q), to ensure that the large-scale atmospheric conditions in the model are close to the observation results, to improve the reliability and accuracy of the model results.

In this article, we make use of the simulation results of domain 03, with the highest horizontal resolution of 1 km, time resolution of 0.5 h, and 34 vertical levels (ground–20 hPa); the coverage of domain 03 is about 200 × 200 km, centred at the Ali Observatory. The vertical distributions of wind at Ali are presented, and the high-altitude wind conditions at the Indian Hanle observatory, which is about 110 km from the Ali Observatory, are also given. Fig. 2 shows the terrain of domain 03 around the Ali Observatory with a resolution of 1 km; the coverage is about 200 × 200 km. The red dot marks the location of the Ali Observatory (80.05°E, 32.30°N, 5050 m), and the red triangle marks the Hanle observatory (78.96°E, 32.78°N, 4500 m) in India.

3 VERTICAL WIND SPEED PROFILES

In order to estimate how well the WRF model analysis performs above the western Tibetan Plateau, we make a comparison of the wind results with the radiosoundings from the closest available radiosonde station, which belongs to the Ali Meteorological Bureau (80.08°E, 32.50°N, 4280 m above sea level), about 25 km north of the Ali Observatory (Qian et al. 2018). The radiosoundings are available at UTC 23:00 (07:00 BT), and UTC 13:00 (19:00 BT), and adding one more time at UTC 05:00 (13:00 BT) in summer, and there were about 320 d of data recorded in 2016. Given the prevalent wind direction in 2016, the Ali Observatory is located in the area covered by the flight paths of balloons in different seasons (Qian et al. 2018). We use the results from radiosoundings of 320 d in 2016 for comparison in this paper, as the time interval of the radiosonde data sets is 1 s, and the WRF results are recorded at 34 vertical levels (ground–20 hPa) according to pressure; as the vertical resolution has been proved to

be the key to estimating optical turbulence with meso-scale models (Basu et al. 2020), we set the vertical resolution of both wind results to 50 m for the wind speed profiles.

To evaluate the statistical reliability of the WRF model, two classical statistical operators, bias and root mean square error (rmse), are introduced, defined as (Masciadri et al. 2013)

$$\text{bias} = \sum_{i=1}^{N} \frac{(Y_i - X_i)}{N} \quad (5)$$

$$\text{rmse} = \sqrt{\sum_{i=1}^{N} \frac{(Y_i - X_i)^2}{N}}. \quad (6)$$

Here, X_i is the individual observed result and Y_i is the individual simulation result at the same time index i; N is the total sample size. The bias and rmse account for all systematic and statistical errors. From the rmse and bias, the bias-corrected rmse (sigma) is deduced as:

$$\text{sigma} = \sqrt{\text{rmse}^2 - \text{bias}^2}. \quad (7)$$

Fig. 3 shows the median profiles of wind speed in 2016 (top), and the difference of the median speed value (middle) and the statistical uncertainty (sigma/$\sqrt{N}$, bottom). Between 11 and 16 km above sea level, the median wind speeds from the model are a bit larger than those from observation. The difference of the median speed value are usually within 2 m s^{-1}, with a relative discrepancy less than or equal to 19 per cent; up to a height of 14–16 km above sea level, the differences of the median values are a bit larger, more than 2 m s^{-1}. For calculating the statistical uncertainty sigma/$\sqrt{N}$, here, $N = 320$, which is the number of days of radiosoundings in 2016. The WRF model analysis provide a reliable estimation of wind speed, and the wind speed profiles are uniformly distributed on a horizontal scale of dozens of kilometres.

In Fig. 4, the rmse and bias are computed on the 320 samples of wind speed obtained from radiosoundings. For the vertical distribution of wind speed, the vertical resolutions of the wind speed profiles from observation and model are interpolated to 50 m, and the bias and rmse at each interpolated height are calculated. The bias values are usually below 1 m s^{-1}, and at the levels of 6–8 km, 14 km and 16–18 km above sea level, they are a bit larger, up to 2 m s^{-1}; the rmse values are 4–8 m s^{-1} below 13 km and above 17 km above sea level, and at the level of 13–17 km above sea level are 8–10 m s^{-1}. In general, we conclude that, for the vertical wind speed, the performance of the WRF model is satisfactory.

In Fig. 5 are shown the monthly quartile vertical wind speed profiles from the WRF model in 2016, from the ground to a height of 25 km above sea level, and the dotted lines mark the heights of 12 and 13 km above sea level, between which the jet stream is located. From the distribution of the global atmospheric circulation, around 30°N, the maximum westerly winds are at 200 hPa, where the subtropical jet stream lies, and the maximum jet stream in the Northern hemisphere is on the east coast of the continent; it is strongest in winter and weakens significantly in summer, while the easterly winds in the tropical regions are strongest and almost continuously surround the whole equatorial region. On the Tibetan Plateau, the geo-potential height that corresponds to 200 hPa has seasonal variations, low in summer and high in winter, varying between 12 and 13 km above sea level (Qian et al. 2018). The upper-level jet stream introduces displacement with the north–south movement of the atmospheric circulation in different seasons, and under the influence of the Hadley circulation, which is strong in winter and weak in summer, the wind speed at the level of the jet stream is liable to change accordingly. In winter, the wind speed is slightly higher than the annual average
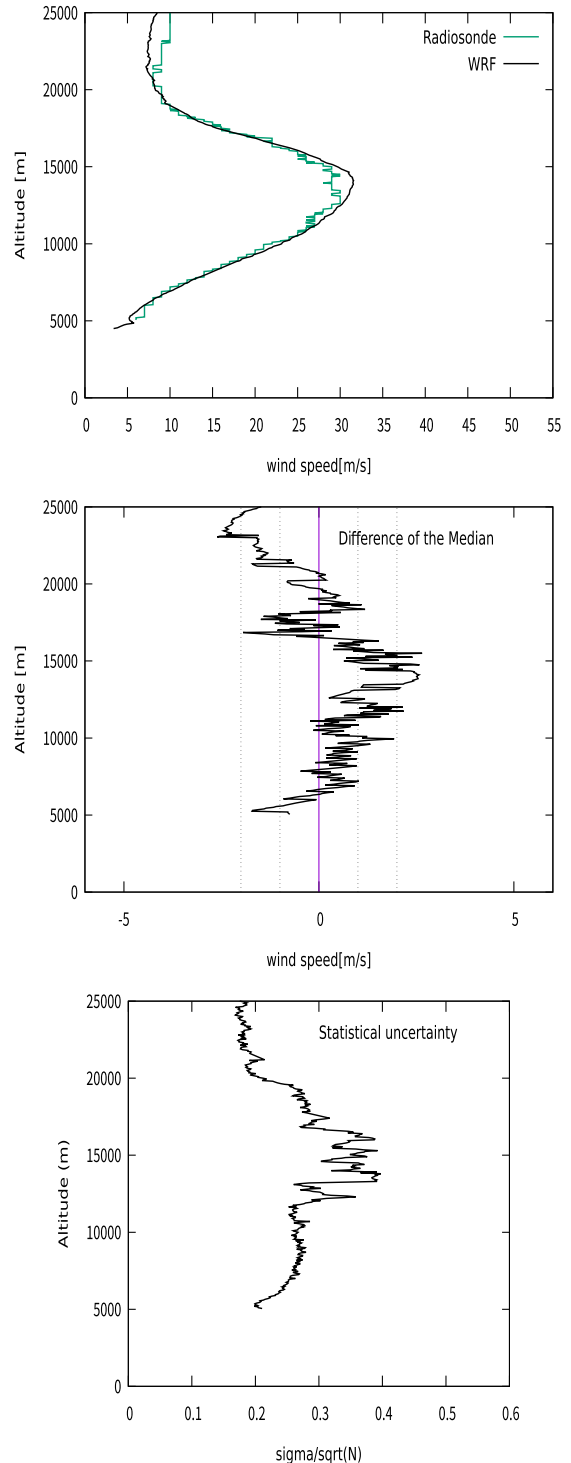

Figure 3. Top: the median profiles of wind speed in 2016 computed from the WRF model and the radiosoundings. Middle: the difference of median wind speeds (radiosoundings, WRF model), with the vertical dotted lines marking the speed interval values of 1 m s^{-1}. Bottom: statistical uncertainty calculated on the 320 samples of 320 d referring to the radiosoundings ($N = 320$). The vertical resolutions of the wind profiles are both set to 50 m.
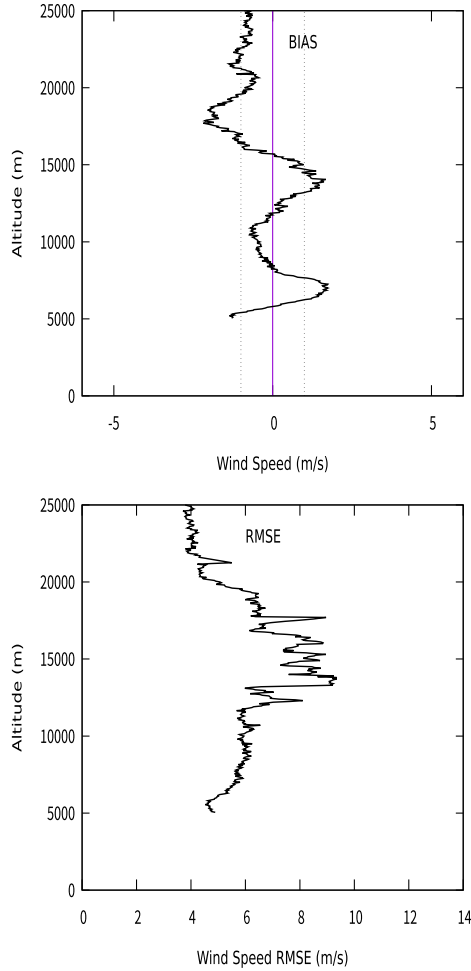
Figure 4. Bias and rmse (WRF model, radiosoundings) of wind speed, with a vertical resolution of 50 m for both profiles; the vertical dotted lines mark the speed interval values of $1\,\mathrm{m\,s^{-1}}$.

value, which corresponds to the strong circulation in winter. The 200 hPa wind speed is lowest throughout the summer, especially in July and August, when the 200 hPa wind speed is much lower than that in other seasons, and the strongest wind speeds are observed above a height of 20 km above sea level.

Figs 6 and 7 show the vertical distributions of monthly median wind speeds and wind directions in 2016 at the Ali Observatory, obtained from the WRF model and radiosoundings. In Fig. 6, the dotted lines in the horizontal direction indicate the characteristic heights of 12 and 13 km above sea level, and the seasonal variations of the 200 hPa wind speed can be clearly observed. In general, the vertical profiles of wind speed and wind direction computed from the WRF model and radiosoundings in each month are broadly consistent.

Generally, in the Northern hemisphere there is a strong mid-altitude upper-level jet stream forming in winter over the southern Pacific and extending into southern China and northern India, covering the southern Tibetan Plateau, that leads to strong high-altitude winds in winter; these are especially strong in February, more than $55\,\mathrm{m\,s^{-1}}$. In summer, the jet stream weakens and moves slightly to the north, and an area of low wind speed covers the Himalayas (Qian et al. 2018). In 2016, the median wind speed was below $15\,\mathrm{m\,s^{-1}}$ in summer at the Ali Observatory, while in the autumn and spring, the median wind speeds were often below $40\,\mathrm{m\,s^{-1}}$.
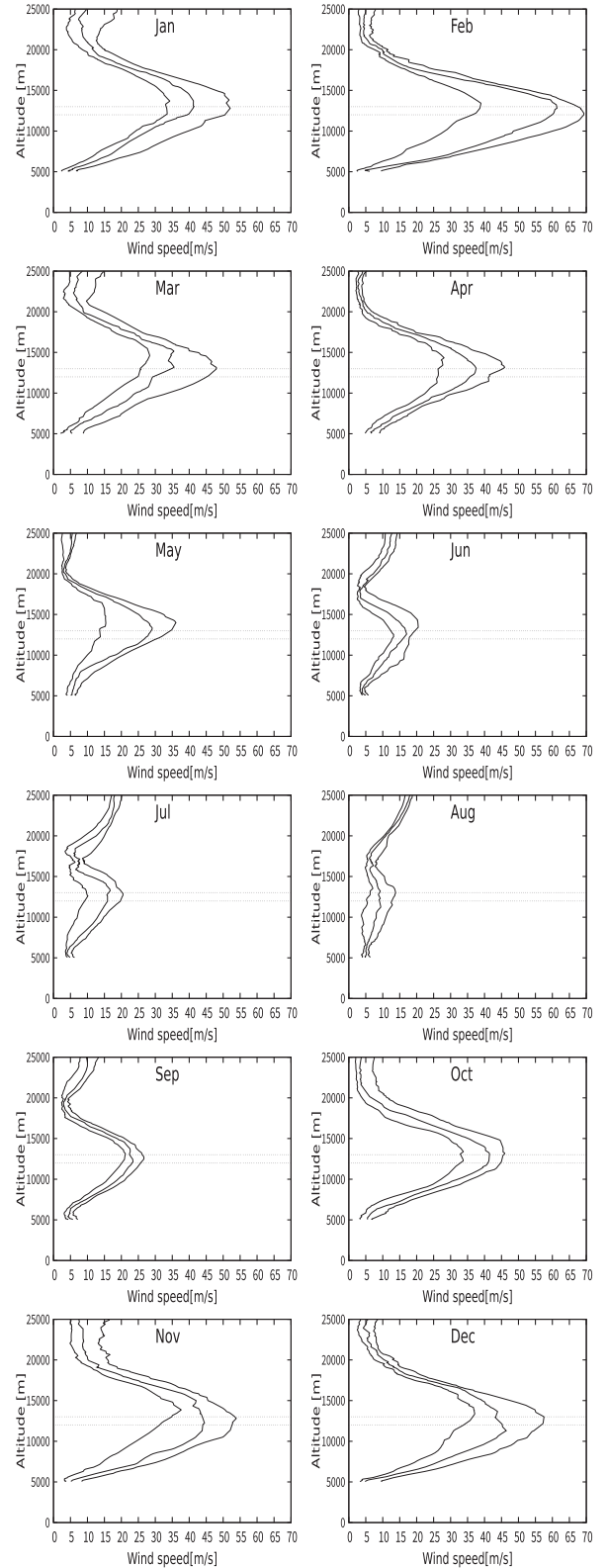

Figure 5. Monthly quartiles of wind speed profiles calculated with the WRF model for each month in 2016 at the Ali Observatory. The dotted lines in the horizontal direction mark the heights of 12 and 13 km above sea level. The vertical resolution of the wind profile is 50 m.
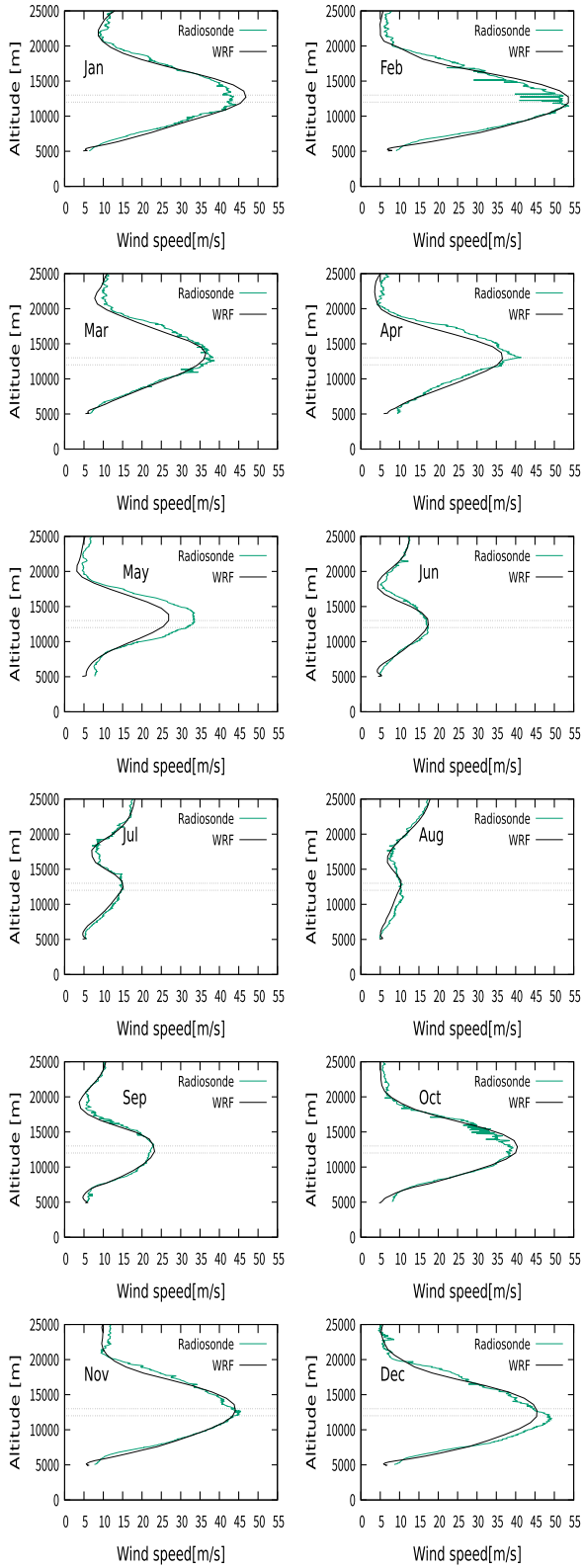
Figure 6. The vertical distributions of monthly mean wind speed profiles during 2016. The green lines represent the wind speed profiles from radiosoundings for comparison. The dotted lines in the horizontal direction mark the heights of 12 and 13 km above sea level. The vertical resolutions of both wind profiles are set to 50 m.
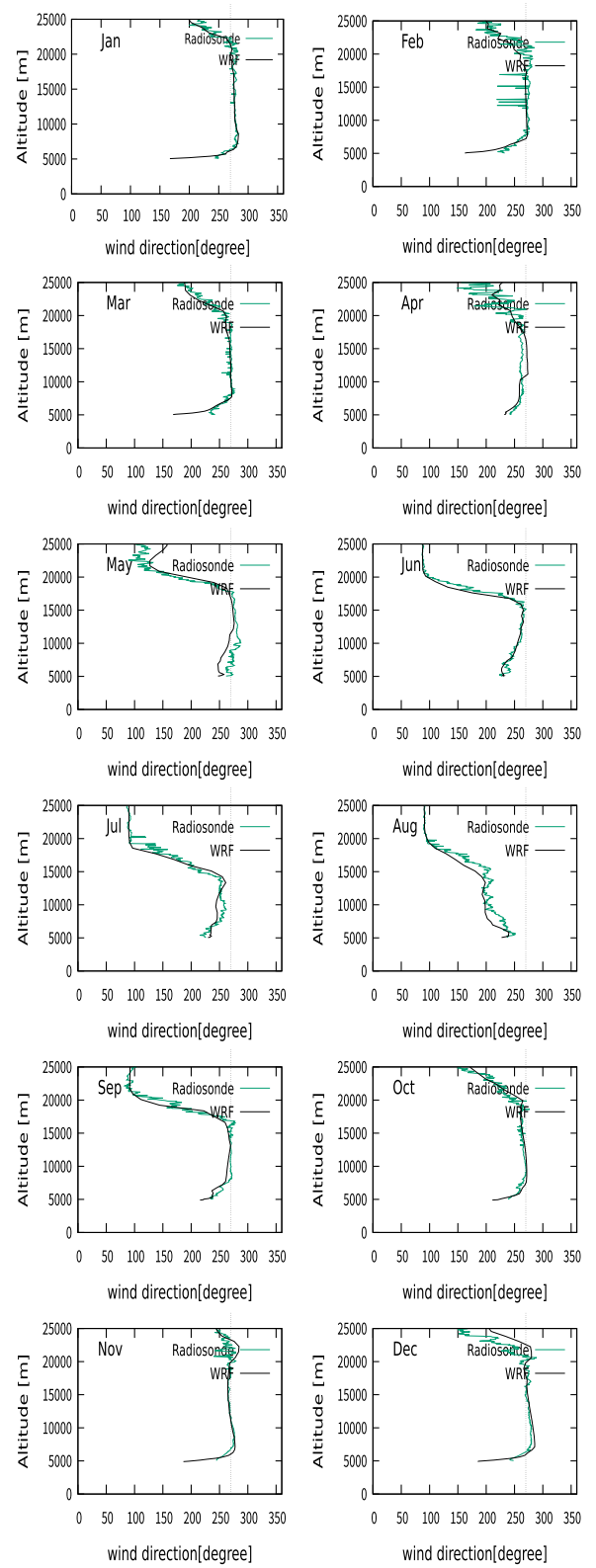
Figure 7. The vertical profiles of monthly mean wind direction in 2016. The green lines represent the wind direction profiles from radiosoundings for comparison. The vertical resolutions of both wind profiles are set to 50 m.

In terms of the global circulation patterns, the 200 hPa subtropics and the mid-latitude areas are westerlies, as the tropics and the two polar regions are easterlies. The dominant wind is a west wind in the troposphere, especially at the jet stream level, and from the the global atmospheric circulation, the wind direction is in line with the prevailing westerlies. The wind direction in August is peculiar, mainly southerly, when the wind speed during this month is the lowest. Above a height of 20 km above sea level, the prevailing wind is easterly from May to September, and southerly between October and March, while there is a west wind in April.

Fig. 8 gives the comparisons of the vertical wind speed profiles at 00 and 12 UTC on one winter day (2016 January 1) and those on one summer day (2016 June 29), respectively. As the radiosonde data set is recorded in 1 s, with more intensive data, while the WRF results are recorded at 34 pressure levels, when we set the resolutions of both data sets to 50 m by interpolation, the wind speed profiles derived from the WRF model are smoother. On the whole, the wind speed profiles from the model are well correlated with the radiosoundings, especially on the summer day, while on the winter day the wind speed varies clearly above 19 km above sea level. The vertical distributions of wind speed at 00 and 12 UTC are basically consistent, while the speed values at 00 UTC are a bit smaller than those at 12 UTC, within $3 \, \mathrm{m \, s^{-1}}$.

4 200 HPA WIND SPEED

In middle latitudes, wind speed varies with height and reaches its maximum at the jet stream level, corresponding to the height of the 200 hPa pressure level (around 12 km above sea level). The high-altitude wind speed varies with the season, as the strongest winds occur in early spring and winter (Masciadri & Garfias 2001; Carrasco, Avila & Carraminana 2005; Lorenzo 2005; Masciadri & Egner 2006; Egner & Masciadri 2007; Bounhir et al. 2009; Masciadri et al. 2010; Hagelin et al. 2010). The strong shear of high-altitude wind speed can cause strong turbulence in the upper air, as atmospheric turbulence can affect the image quality of a telescope, and adaptive optics can be used to compensate for atmospheric turbulence, which allows telescopes to reach their diffraction resolution limits. Therefore, the 200 hPa wind speed is a key factor that affects the observation conditions of an observatory site and is applied to evaluate the adaptive optical conditions of ground-based telescopes. The 200 hPa wind speed has often been used to retrieve the conditions of the wavefront coherence time (τ_0) and the frequency limitations of instruments based on AO systems.

From the conclusions of the preliminary remote study of the site testing in China (Zhang et al. 2012; Yao et al. 2012; Qian et al. 2018), which are obtained from the national radiosonde data sets, we can conclude that the 200 hPa wind speed near the upper jet stream in the eastern coastal area of China is relatively large, and it decreases to the north, west and south directions; the seasonal variation of the 200 hPa wind speed is obvious, as the centre of jet stream moves to the north-west of China in summer, and the intensity decreases clearly, while in the winter half year the centre is located at the east coast with a larger intensity; on the whole, the 200 hPa wind speed in the area above 40°N and its northern region shows little seasonal and vertical variation and weak convection, while in the south of China, the 200 hPa wind speed has great seasonal and vertical variations and also strong convection.

Fig. 9 presents the seasonal distributions of the 200 hPa wind fields. In this area, a coverage of 200 × 200 km, are the Ali Observatory (80.05°E, 32.32°N, 5050 m above sea level) in China located on
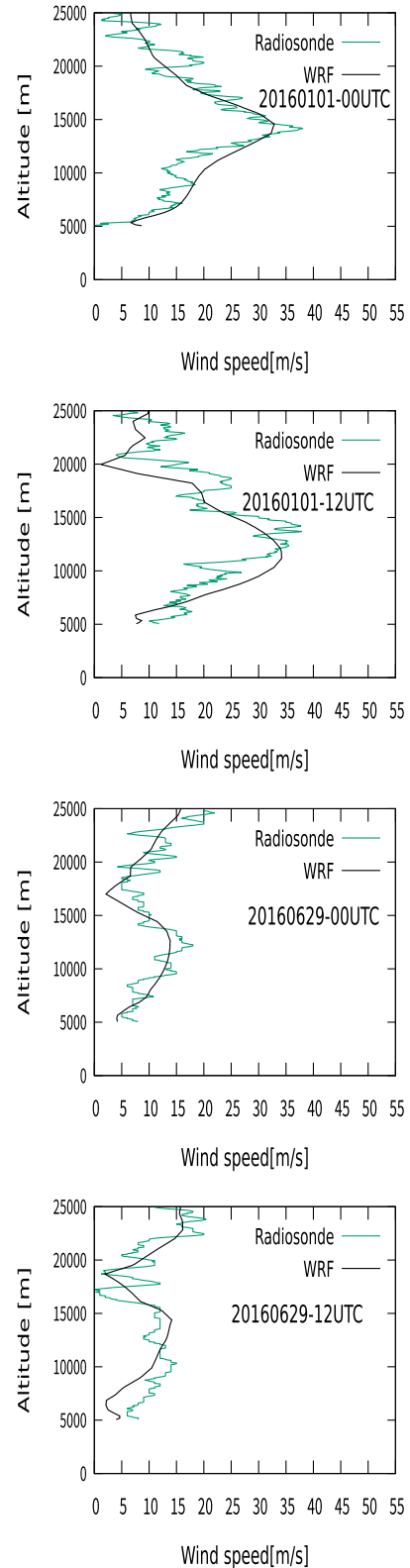

Figure 8. The vertical distributions of median wind speed profiles at 00 and 12 UTC during two selected days. The green lines represent the wind speed profiles from radiosoundings for comparison. The vertical resolutions of both wind profiles are set to 50 m.
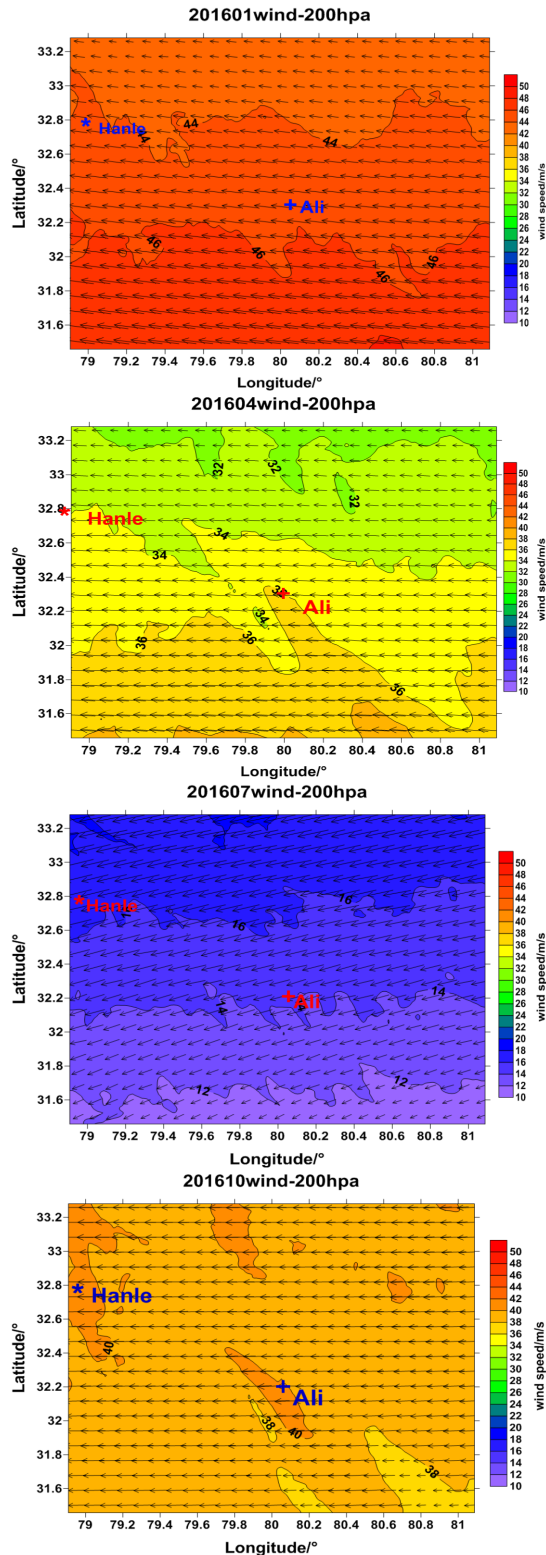
Figure 9. The seasonal distributions of 200 hPa wind fields obtained from the WRF model around the Ali Observatory in January, April, July and October, which represent winter, spring, summer and autumn respectively. The coverage is 200 × 200 km, centred at (80.08°E, 32.30°N). The '+' marks the location of the Ali Observatory, and the '⋆' marks the Hanle observatory. The contours in different colours represent wind speed values, the colour bar on the right-hand side indicates the wind speed value in units of m s⁻¹, and the '←' indicates the wind direction at 200 hPa.

Table 2. The yearly and monthly median wind speeds and directions at 200 hPa at Ali and those at Hanle.

Month	Ali		Hanle	
	wind speed /m s^{-1}	wind direction/°	wind speed /m s^{-1}	wind direction/°
Jan	38.84	274.42	37.13	275.28
Feb	60.96	270.45	57.89	269.81
Mar	29.27	271.73	30.39	268.79
Apr	36.39	269.10	33.98	267.55
May	27.56	279.84	27.81	280.25
Jun	16.76	262.61	16.81	262.58
Jul	15.64	252.48	16.70	251.86
Aug	9.27	213.28	11.61	222.03
Sep	23.53	267.01	23.75	267.06
Oct	41.87	269.73	42.48	268.98
Nov	43.95	269.92	45.01	270.39
Dec	45.09	276.94	48.27	275.39
yearly	33.60	272.51	31.60	272.36

the northern side of the Himalayas and the Indian Astronomical Observatory, Hanle (78.96°E, 32.78°N, 4500 m above sea level) (Ananthasubramanian, Yamamoto & Prabhu 2002; Ningombam, Jade & Shrungeshwara 2016), an infrared observatory very close to the Ali Observatory, located on the other side of the Himalayas. The spatial distributions of the 200 hPa wind fields in different seasons are presented for evaluating the adaptive optical conditions at the sites (Vernin 1986; Sarazin & Tokovinin). In different seasons, we can observe that the high-altitude wind speed varies little in this area, and it is uniform on a horizontal scale of dozens of kilometres above the broad plateau.

From the global atmospheric circulation, westerlies prevail in the 200 hPa subtropical and mid-latitude regions, and easterly winds prevail in the tropics and the poles. Around 30°N, the 200 hPa westerly wind speed is largest, where the subtropical jet is located, and it is strongest in winter and significantly weakened in summer. In summer, the 200 hPa wind speeds are obviously small in this region, below 22 m s⁻¹; at Ali, the 200 hPa wind speeds are almost below 16 m s⁻¹ and are prevailing north winds, which are lower than those at Hanle, where the value is around 20 m s⁻¹ and they are prevailing west winds. In spring and winter, the 200 hPa wind speeds are usually large: in spring, the 200 hPa wind speed values are 30–40 m s⁻¹; at Ali, the 200 hPa wind speed values are around 40 m s⁻¹, prevailing north-east, while the speeds at Hanle are about 43 m s⁻¹ with a south wind; in winter, the 200 hPa wind speeds are about 45 m s⁻¹, prevailing south-west, while the south wind speeds are around 42 m s⁻¹ at Hanle.

Table 2 gives the monthly median 200 hPa wind speeds at the Ali Observatory and those at Hanle. The yearly median 200 hPa wind speed at Hanle is about 31.6 m s⁻¹, contrasting with 33.6 m s⁻¹ at Ali, and the prevailing wind directions are almost west winds, which is consistent with the distribution of the 200 hPa jet stream. In winter, the 200 hPa wind speed is largest, above 35 m s⁻¹, prevailing west; in autumn and spring, the 200 hPa wind speed values are 25–40 m s⁻¹, prevailing west. The 200 hPa wind speeds are small in summer, below 20 m s⁻¹, especially in August when the smallest 200 hPa wind speed at Ali is below 10 m s⁻¹ and 11.6 m s⁻¹ at Hanle, prevailing south-west, which is in line with the distribution of the prevailing westerlies in the upper air and the global circulation.

In Fig. 10 is shown a comparison of the average 200 hPa wind speed at the Ali site with those at some other observatories (Carrasco & Sarazin 2003; Chueca et al. 2004); we need to shift by six months
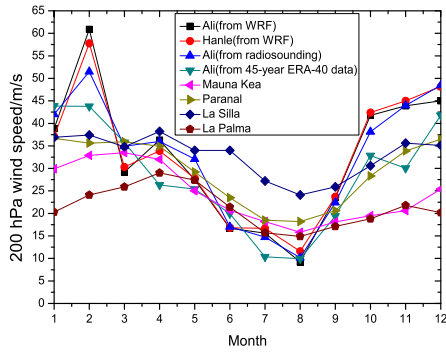
Figure 10. Seasonal variations of the 200 hPa wind speed at the Ali site and other observatories.
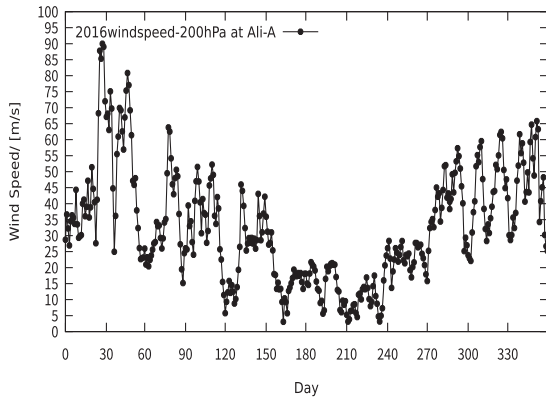

Figure 11. Distribution of daily 200 hPa wind speed from the WRF model for the whole of 2016 at Ali. The *x*-axis is the number of days in 2016.

for the La Silla and Paranal sites in the Southern hemisphere on account of summer in the Northern hemisphere corresponding to winter in the Southern. A long-term statistic of more than 45 yr of the monthly mean behaviour of the 200 hPa wind speed at the Ali Observatory is also given; the time span is from 1957 September to 2002 August. This was obtained by atmospheric data assimilation of the ERA-40 reanalysis data, with a spatial resolution of 2.5° (Uppala et al. 2005; Qian et al. 2018). At Ali, the 200 hPa wind speed simulated by the model in 2016 is basically consistent with the measured mean speed, while the 45-yr average trendline is slightly lower than the simulated one. Compared with other observatories, the 200 hPa wind speed at the Ali Observatory is relatively large, and is lowest in summer (about 10 m s^{-1}) and strongest in winter (larger than 40 m s^{-1}), while the speed values vary between 17 m s^{-1} and 38 m s^{-1} at other observatories. The low 200 hPa wind speed in the summer half year reveals that the Ali site has the potential advantage of low seeing in summer for adaptive optics observations if the turbulence in the lower atmosphere can be reasonably reduced to a minimum.

4.1 200 hPa wind speed at Ali

In Fig. 11 is shown the distribution of 200 hPa wind speed values obtained from the WRF model in 2016 at the Ali site. In summer, the 200 hPa wind speed is smallest, below 20 m s^{-1}; in winter, the upper-level wind speed varies from 20 to 65 m s^{-1}, especially in February, when the largest wind speed is up to 80 m s^{-1}; in spring, the 200 hPa wind speeds are 25–55 m s^{-1}.
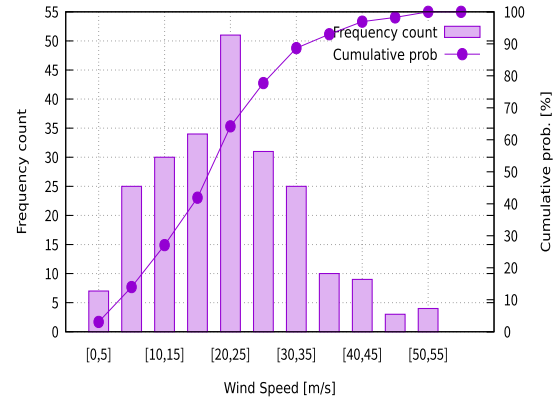

Figure 12. Monthly quartile values of 200 hPa wind speed in 2016 at Ali; the histograms show the median and the vertical bars indicate quartiles of wind speeds.
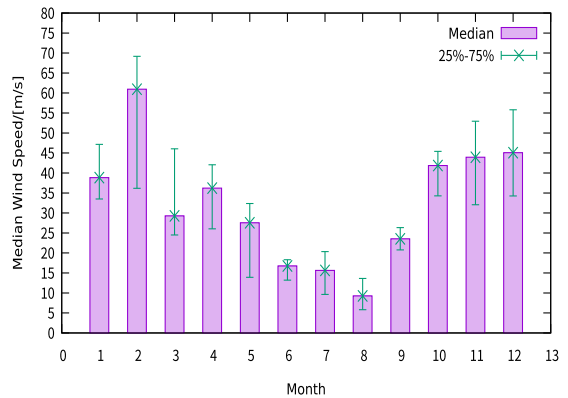

Figure 13. Histogram and cumulative probability distribution of 200 hPa wind speed in 2016 at Ali, from the results of the WRF model.

Fig. 12 displays the monthly quartile values of the 200 hPa wind speed derived from the WRF model in 2016 at the Ali site. The weakest wind is observed in summer, the strongest in spring. In February, the largest speed values are 60–65 m s^{-1}. The median 200 hPa wind speed is about 20 m s^{-1}, and is around 10 m s^{-1} in August. In the winter, the median speed is between 40 and 50 m s^{-1}. In Fig. 13 is shown the cumulative distribution and histogram of the 200 hPa wind speeds in 2016 at Ali. The median 200 hPa wind speed in 2016 was about 33.6 m s^{-1} at the Ali Observatory, slightly higher than that from radiosounding measurements in 2016 (31.2 m s^{-1}) (Qian et al. 2018); during this year, nearly 65 per cent of the 200 hPa wind speeds were lower than 25 m s^{-1}, and the simulated 200 hPa wind speeds lower than 50 m s^{-1} were up to 100 per cent of the time.

4.2 200 hPa wind speed at Hanle

Fig. 14 gives the distribution of daily 200 hPa wind speed from the WRF model in 2016 at Hanle. In this year, the 200 hPa wind speeds are basically below 70 m s^{-1}; the smallest upper-level wind speeds appear in summer, below 25 m s^{-1}, a bit larger than those at Ali, and in winter, the 200 hPa wind speeds are from 20 to 65 m s^{-1}; in spring, the largest speeds are 20–80 m s^{-1}; in particular, the maximum value appearing in January was up to 90 m s^{-1}.

Fig. 15 presents the monthly quartiles of the 200 hPa wind speed derived from the WRF model in 2016 at Hanle. In February, the
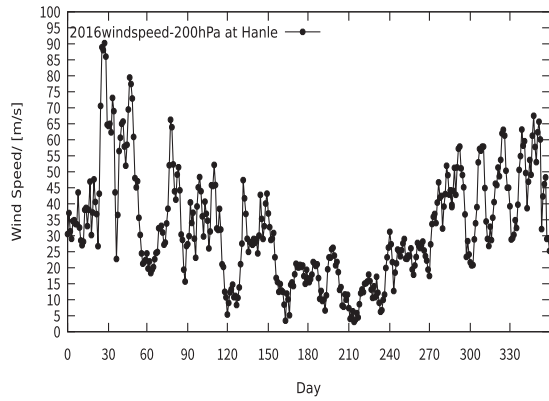
Figure 14. Distribution of daily 200 hPa wind speed from the WRF model for the whole of 2016 at Hanle. The *x*-axis is the number of days in 2016.
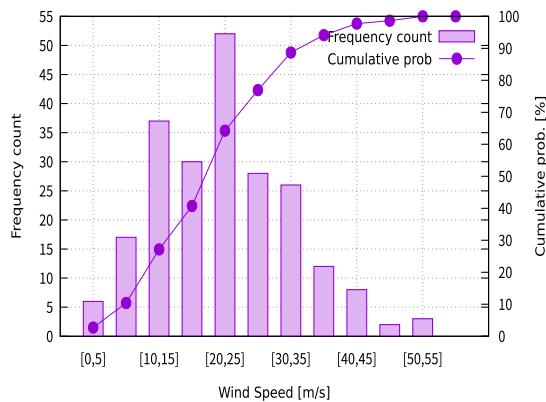

Figure 15. Monthly quartile values of 200 hPa wind speed in 2016 at Hanle; the histogram shows the median and the vertical bars indicate quartiles of wind speeds.
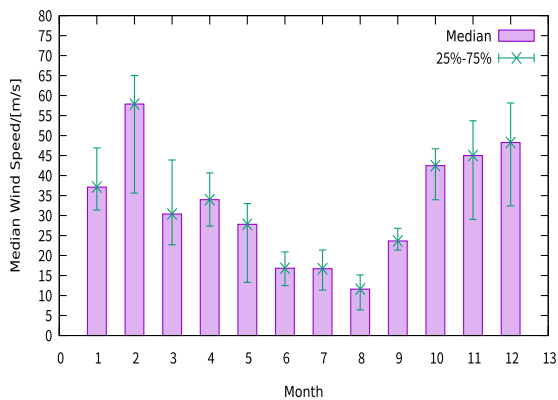

Figure 16. Histogram and cumulative probability distribution of 200 hPa wind speed in 2016 at Hanle, from the results of the WRF model.

largest 200 hPa wind speed is up to 60 m s^{-1}, and in winter, the upper-level wind speeds vary between 45 and 50 m s^{-1}; in summer, the smallest wind speeds are 15–20 m s^{-1}, being in particular lower than 15 m s^{-1} in August. Fig. 16 shows the cumulative distribution and histogram of the 200 hPa wind speed in 2016 at Hanle. In this year, with nearly 65 per cent of the 200 hPa wind speeds lower than 25 m s^{-1}, 200 hPa wind speeds lower than 35 m s^{-1} were simulated nearly 90 per cent of the time.
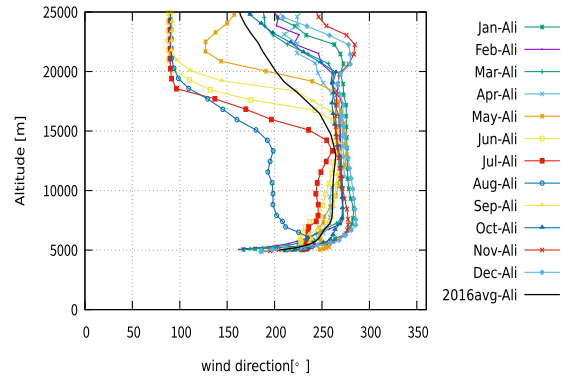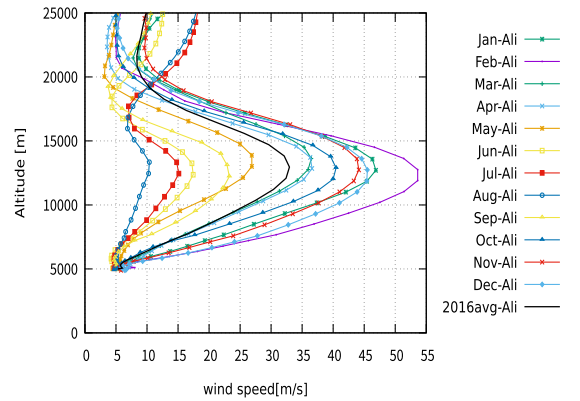

Figure 17. The vertical profiles of yearly and monthly average wind speed and direction in 2016 at Ali.

Figs 17 and 18 display the vertical distributions of yearly and monthly mean wind speed and wind direction in 2016 at the Ali Observatory and Hanle, respectively. The vertical distribution trends of wind speed and direction at Ali and those at Hanle are consistent, which indicates that the high-altitude wind is uniform on a horizontal scale of dozens of kilometres in different seasons in a certain area above the plateau.

From the profiles, the seasonal variations of wind speed in the tropopause can be clearly observed. Below 200 hPa, the wind speed increases with height; from 200 hPa to 20 km above sea level, the wind speed decreases sharply and then begins to increase steadily in most seasons. The prevailing winds are westerlies in the tropopause, especially at 200 hPa. In August, the wind speed is at its lowest during the year, and the wind direction is peculiar, being mainly southerly winds.

In January, a strong mid-latitude upper-level jet stream forms and covers the southern Tibetan Plateau, leading to the strongest high-altitude wind in winter, with speeds up to 55 m s^{-1} in February. In summer, the jet stream weakens and moves a little bit to the north, and low wind speeds cover the Himalayas. At Ali, the maximum mean wind speeds vary from 10 to 18 m s^{-1} in summer; in autumn and spring, the maximum mean wind speeds are about 35–45 m s^{-1}. Hanle is located in the southern part of the Himalayas, and the maximum mean wind speeds vary from 5 to 15 m s^{-1} in summer, while in autumn and spring, the maximum mean wind speed values are about 37–45 m s^{-1}. Obviously, the maximum high-altitude wind speed in summer at Hanle is a bit lower than that at Ali, while in winter the maximum wind speed at Hanle is slightly larger than that at Ali. On the whole, the distribution of high-altitude wind in this area is homogeneous.
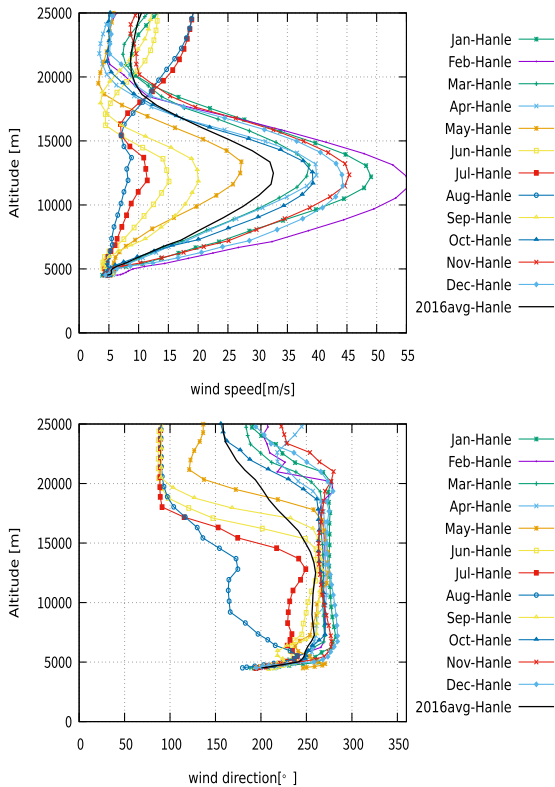
Figure 18. The vertical profiles of yearly and monthly average wind speed and direction in 2016 at Hanle.

5 CONCLUSIONS

In this paper, we summarize the characteristics of the vertical distributions of wind speed and direction in the Ali region, above the western Tibetan Plateau. By using the meso-scale numerical WRF model, we obtain the characteristics of the vertical wind speed profiles at the Ali Observatory, using the ERA-Interim reanalysis data sets (with a spatial resolution of 0.75°) in 2016. There are three domains nested in the WRF model configuration, the spatial resolution of the inner domain (d03) is 1 × 1 km, which covers an area of 200 × 200 km, and the time resolution is 0.5 h. We obtain the wind fields at 200 hPa in this area, and the wind speed profiles at the Ali Observatory (80.05°E, 32.32°N, 5050 m above sea level) and those at the Indian Hanle observatory (78.96°E, 32.78°N, 4500 m above sea level) located on both sides of the Himalayas are also presented. The direct way of retrieving a complete characterization of the wind speed profile is radiosoundings. In this study, a detailed analysis was performed at the Ali site in 2016, showing reliable performances with that corresponding to the radiosoundings from the nearby Ali Meteorological Radiosonde Station. The WRF model has been proved to be good at simulating the wind conditions above the Ali Observatory.

As the WRF model is proved to be reliable, we present the vertical distributions of monthly median wind speed in the whole of 2016. The vertical distributions of wind speed accord with the characteristics of typical mid-latitude sites with an evident maximum wind speed at 200 hPa (about 12–13 km above sea level on the Tibetan Plateau). In summer, the strongest wind occurs in the stratosphere; the largest variations of median speed are observed in spring and autumn. The 200 hPa wind speed is one of the key parameters for evaluating the adaptive optical conditions at an observatory site. The yearly

median 200 hPa wind speed was about 33.6 m s^{-1} in 2016 at the Ali Observatory, prevailing west; at Hanle, the yearly median 200 hPa wind speed was about 31.6 m s^{-1}, prevailing west. The upper-level wind speed is small in summer; the values at Ali are 8–17 m s^{-1}, while they are a bit larger (10–17 m s^{-1}) at Hanle. In autumn and winter the upper-level wind is strong, with values between 40 and 65 m s^{-1}, while the speeds at Hanle are a bit smaller, 40–60 m s^{-1}; in January, the 200 hPa wind speeds at both sites are around 38 m s^{-1}. These are all similar to the distribution of the global atmospheric circulation, as the region is located in the centre of the subtropical upper-level jet stream, with prevailing westerlies. In addition, the largest 200 hPa wind speeds at both sites appear in February, above 55 m s^{-1}. From the seasonal distributions of the 200 hPa wind fields, we can observe that the high-altitude wind speed varies little in an area, and it is uniform on a horizontal scale of dozens of kilometres above the plateau in different seasons.

From the wind profiles at the Ali Observatory and Hanle, the obviously seasonal variations of the maximum wind speeds at the height of the tropopause are presented, and the prevailing wind directions in the troposphere are west winds. Affected by mid-latitude westerlies, westerlies prevail in the tropopause and the wind speed is relatively high. From the ground surface layer to the tropopause, the wind speed increases with height, and decreases above the tropopause. In summer, the vertical variations of the wind profiles are a bit smaller than those in other months and the wind speed values are also small, while in autumn and winter, the variations of the vertical profiles are large, with large wind speed values.

Moreover, we evaluate the performance of the meso-scale WRF model in characterizing the vertical wind profile above the western Tibetan Plateau, from the ground surface layer to the top. The wind profile obtained from the model agrees well with that from the radiosonde measurements, indicating that the model method can systematically simulate the vertical distribution of wind at a site, even in the ground surface layer. Wind simulations provided by the WRF model will be of great benefit for adaptive optics, which also provides the vertical distribution of C_N^2 and τ_0 at astronomical observatories. In summary, the Ali Observatory has the potential advantage of small seeing for adaptive optics observation, especially in the summer half year. Studies on the atmospheric turbulence conditions at the Ali Observatory are also in progress, and the results will be published soon.

DATA AVAILABILITY

The radiosounding data in this article are provided by the Ali Meteorological Bureau and the China Meteorological Administration under licence and the data will be shared on request to the corresponding authors with permission of the Ali Meteorological Bureau. The ERA-Interim reanalysis data for the initial and boundary conditions for the configuration of the WRF model are available from https://www.

ecmwf.int/en/forecasts/datasets/reanalysis-datasets/era-interim, re-
leased by the European Center for Medium-Range Weather Forecasts
(ECMWF) .

REFERENCES

Ananthasubramanian P., Yamamoto S., Prabhu T., 2002, in Vernin J.,
    Benkhaldoun Z., Muñoz-Tuñón C., eds, Astronomical Site Evaluation
    in the Visible and Radio Range. ASP Conference Proceedings, Vol. 266.
    Astronomical Society of the Pacific, San Francisco, p. 164
Basu S., Osborn J., He P., DeMarco A. W., 2020, MNRAS, 497, 2302B
Bounhir A., Benkhaldoum Z., Carrasco E., Sarazin M., 2009, MNRAS, 398,
    862
Carrasco E., Sarazin M., 2003, Rev. Mex. Astron. Astrofis. Serie Conf., 19,
    103
Carrasco E., Avila R., Carraminana A., 2005, PASP, 117, 104
Chueca S., García-Lorenzo B., Muñoz-Tuñón C., Fuensalida J. J., 2004,
    MNRAS, 349, 627
Egner S. E., Masciadri E., 2007, PASP, 119, 1441E
García-Lorenzo B., Fuensalida J. J., Muñoz-Tuñón C., Mendizalbal E., 2005,
    MNRAS, 356, 849
Hagelin S., Masciadri E., Lascaux F., 2010, MNRAS, 407, 2230H
Jordan P. G., Almazan C. J. A., Tunon M. C., Codina B., Vernin J., 2015,
    MNRAS, 452, 1992
Li F., Zou H., Zhou L. B., Ma S. P., Li P., Zhu J. H., Zhang Y., 2017, Plateau
    Meteorology, 36, 340 [in Chinese]
Masciadri E., 2003, Rev. Mex. Astron. Astrofis., 39, 249M
Masciadri E., Egner S., 2006, PASP, 118, 1604
Masciadri E., Garfias T., 2001, A&A, 366, 708
Masciadri E., Stoesz J., Hagelin S., Lascaux F., 2010, MNRAS, 404, 144
Masciadri E., Lascaux F., Fini L., 2013, MNRAS, 436, 1968
Ningombam S. S., Jade S., Shrungeshwara T. S., 2016, J. Atmos. Sol. Terr.
    Phys., 137, 76

Qian X., 2011, Sci. Sinica Phys. Mech. Astron., 41, 896 [in Chinese]
Qian X., Yao Y. Q., Wang H. S., Liu L. Y., Li J. R., Yin J., 2015, J. Phys.
    Conf. Series, 595, 012028
Qian X., Yao Y.Q., Wang H.S., Wang Y. P., Bai Z., Yin J., 2018, PASP,
    130l5002Q
Qian X., Yao Y. Q., Zou L., Wang H. S., Yin J., 2019, PASP, 131123001
Roddier F., 1981, Progress Opt., 19, 281R
Roddier F., Gilli J. M., Lund G., 1982, J.Opt., 13, 263R
Sarazin M., Tokovinin A., 2001, in Vernet E., Ragazzoni R., Esposito
    S., Hubin N., eds, ESO Conf. Workshop Proc. 58, Beyond Conven-
    tional Adaptive Optics. European Southern Observatory, Garching bei
    München, p. 321
Sivo G., Turchi A., Masciadri E., Guesalaga A., Neichel B., 2018, MNRAS,
    476, 999
Uppala S. M. et al., 2005, Q. J. R. Meteorological Soc., 131, 2961
Vernin J., 1986, SPIE, 628, 142V
Wang H. S., Yao Y. Q., Qian X., Liu L. Y., Wang Y. P., Li J. R., et al. 012,
    Acta Astron. Sinica, 53, 527 [in Chinese]
Xu L. J., Liu H. Z., Xu X. D., Du Q., Wang L., 2018, Acta Meteorologica
    Sinica, 76, 955 [in Chinese]
Yang X. H., Zhaxi Y. Z., Zhuo G., Bianba C. R., 2008, Acta Prataculturae
    Sinica, 17, 102 [in Chinese]
Yao Y. Q., Wang H. S., Liu L. Y., Wang Y. P., Qian X., Yin J., 2012, SPIE,
    8444, 1
Zhang Y., Wang P.X., Yao Y. Q., Wang G. F., Liu L. Y., Qian X., 2010, Sci.
    Sinica Phys. Mech. Astron., 40, 1302 [in Chinese]
Zhang Y., Yao Y. Q., Qian X., Liu L. Y., Wang H. S., 2012, Sci. Sinica Phys.
    Mech. Astron., 42, 1 [in Chinese]

This paper has been typeset from a TEX/LATEX file prepared by the author.